POLITECNICO DI TORINO
Repository ISTITUZIONALE

Experimental investigation of Triply Periodic Minimal Surfaces for high-temperature solar receivers

(Article begins on next page)

21 November 2024
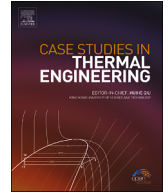
Experimental investigation of Triply Periodic Minimal Surfaces for high-temperature solar receivers

A. Mortazavi [a], A.L. Ávila-Marín [b], H. Ebadi [a], E. Gajetti [a], C. Piatti [a], L. Marocco [c, *], L. Savoldi [a]

[a] *Dipartimento Energia "Galileo Ferraris", Politecnico di Torino, Torino, Italy*
[b] *Point-Focus Concentrating Solar Thermal Technologies, CIEMAT, Madrid, Spain*
[c] *Dipartimento di Energia, Politecnico di Milano, Milano, Italy*

HIGHLIGHTS

- Two planar solar receivers manufactured in stainless steel with TPMS lattices.
- Receivers were tested in a solar simulator and compared experimentally.
- Effects of mass flow rate and heat flux were analyzed.
- The sample with SplitP lattice showed higher thermal and exergy performance.

ARTICLE INFO

ABSTRACT

This study experimentally investigates Triply Periodic Minimal Surfaces (TPMS) as structured porous media for concentrated solar power systems. Two mock-up planar solar receivers with different TPMS lattices, Diamond and SplitP, were fabricated using Additive Manufacturing. Testing was conducted within the SFERA III project, funded by the EU, utilizing a solar simulator facility at IMDEA Energy Institute in Madrid, Spain. Thermal performance was evaluated under varying mass flow rates and heat flux levels, using synthetic air as the working fluid. Results show superior performance of the SplitP lattice over the Diamond lattice, exhibiting higher heat absorption, lower heat loss, and improved thermal and exergetic efficiencies. SplitP achieved a maximum thermal efficiency of approximately 70 %, compared to 60 % for Diamond, and an exergetic efficiency of approximately 12 %, compared to 8 % for Diamond.

1. Introduction

The urgent need for clean energy has promoted rapid development of renewables. By the end of 2023, renewable energy sources accounted for 43 % of the total global installed power capacity [1]. Solar energy stands out as the most abundant and widely dispersed renewable energy source available [2] and among solar technologies, concentrated solar power (CSP) is seen as a promising technology [3–5]. In CSP technologies, solar thermal energy is concentrated on a focal line or point using different configurations of mirrors or concentrators to attain medium-to-high temperatures. The concentrated heat is then removed by a heat transfer fluid (HTF) and can be subsequently converted to electricity in the conventional power cycles.

To increase the efficiency of CSP technologies, numerous studies have been done on possible modifications to the receiver to increase the heat transfer surface and/or promote turbulence [6], on the usage of different heat transfer fluids [7,8] or on the usage of nano fluids [9] to increase the thermal properties of the HTFs, or on development of different coating with the aim of improving optical efficiency [10,11]. For instance, Wang et al. [12] studied the thermohydraulic performance of the receiver of a parabolic trough collector (PTC) partially/fully filled with high porosity metal foams. They evaluated the effect of the layout of metal foam (placed either at the top or at the bottom of the receiver), geometrical parameter and porosity, and in their optimum thermohydraulic configuration, compared to a smooth receiver tube, the Nusselt number increased 5–10 times, paid at the cost of an increase of the friction factor of 10–20 times. Mwesigye et al. [13] investigated the performance of a PTC's receiver with perforated-plate inserts, exploring different plate diameters, orientation angle and spacing with a given porosity of 0.65. For their considered range of Reynolds numbers, temperatures and geometrical parameters, they managed to achieve an improvement of >130 % in the Nusselt number, with a friction factor increase up to 95 times compared to a smooth receiver tube. In an experimental effort, Jamal-Abad et al. [14] investigated a parabolic through receiver filled with a copper metal foam. Although the porous medium reduced the overall loss coefficient by 45 % and increased the thermal efficiency, a considerable increase in friction factor was reported. In a numerical and experimental study, Savoldi et al. [15] investigated the usage of Raschig Rings as porous medium in a planar solar receiver using air as HTF. From their results, they concluded their tested configuration had an improvement in the heat transfer by a factor of around 5 and a Thermal Enhancement Factor (TEF) of 2–2.5 when compared to the same receiver configuration but without Raschig Rings. Considering again Raschig Rings as the porous medium within a solar receiver, Ebadi et al. [16,17] also conducted an experimental and numerical research on tubular receivers, observing that their unstructured porous insert increased the thermal efficiency. However, they also observed dead zones in which the flow was stagnant: the unstructured porous medium in fact affects the fluid at the macroscopic level by creating non-uniform flow fields with considerably different velocities [18]. Overall, although unstructured porous inserts substantially increase the thermal performance in the receivers, they also cause an increase in pressure drop which requires considerably higher pumping power. A comparison between conventional unstructured porous media and structured lattices was carried out by Tian et al. [19,20]. In their experimental and theoretical study, they found that the adopted copper textile structures performed as well as the stochastic metal foams (aluminium and copper based), but with a substantially lower pumping power. Additionally, the overall thermal efficiency of the studied textile-based structures was found to be three times higher than that of copper foams with a comparable weight. Regrettably, structured porous media utilized as inserts within solar receivers have not received adequate attention in the literature.

Triply Periodic Minimal Structures (TPMS) offer several advantages for solar receivers, making them promising candidates for enhancing the efficiency and durability of concentrated solar power (CSP) systems:

- Versatility in design, reduced material usage and superior mechanical strength: additive manufacturing techniques allow precise customization of TPMS [21] for specific thermal and mechanical requirements in CSP applications. Moreover, TPMS achieve strength and thermal performance with less material, leading to cost savings and lighter solar receivers. Their robust structural design [22] allows TPMS to withstand high thermal stresses and harsh conditions, increasing the lifespan of solar receivers with reduced maintenance.
- High surface area-to-volume ratio: TPMS enhance heat transfer by providing extensive surface area-to-volume ratio [23] for efficient absorption and distribution of solar energy, improving thermal performance.
- Optimized fluid dynamics and improved heat transfer: TPMS structures optimize fluid flow, reducing pressure drops and preventing the occurrence of the dead zones [24], thus enhancing convective heat transfer and resulting in more effective cooling. TPMS facilitate uniform heat distribution, reducing hotspots and minimizing thermal losses [25].

By leveraging these advantages, TPMS can significantly improve the thermal efficiency, mechanical reliability, and overall performance of solar receivers, making them valuable for next-generation CSP systems.

Khalil et al. [26] compared the performance of two lattices constituted by specific TPMS topologies, namely Diamond and Gyroid, with three other heat sinks, concluding that the Diamond sample showed higher thermal efficiency. Modrek et al. [27] analyzed the thermal performance, such as effective thermal conductivity, of TPMS-based heat sinks. They designed heat sinks using the topology optimization technique and proposed two mapping approaches to transform porous cellular structures to Gyroid-based heat sinks, analyzing and comparing the heat transport therein. Yan et al. [28] studied experimentally the thermohydraulic performance of different TPMS lattices - namely Gyroid, Diamond, Primitive - and their two-by-two combinations (Gyroid/Diamond, Diamond/Primitive and Gyroid/Primitive). To compare the overall performance of each lattice (considering both pressure drop and heat transfer) in the studied range of air flow Reynolds numbers (400–1200), they adopted an area goodness factor, defined as the ratio of Colburn factor to friction factor. The Gyroid lattice resulted in the highest ratio in view of its low pressure drop, but the Diamond lattice had the highest heat transfer coefficient. Another work of Modrek et al. [29] based on a multi-objective optimization of four TPMS structures, namely Gyroid, Diamond, Primitive, and IWP, highlights the potential of Diamond TPMS in improving both thermal and mechanical performance of passive heat sinks.

Although TPMS lattices have garnered attention in heat exchangers or as heat sinks for high heat flux removal [30], their efficacy as heat sinks in concentrated solar power applications has not been extensively studied. To explore the potential utilization of TPMS structures in enhancing heat transfer in high-temperature solar receivers, two mock-ups of planar solar receivers equipped with different TPMS lattices were designed, manufactured, and subjected to testing to determine their thermal performance under various mass flow rates and concentrated heat fluxes. According to the above literature review, the Diamond lattice emerged as a promising candidate for effective heat removal, leading to its selection for the first mock-up. The second chosen lattice was the SplitP, which has only recently gained attention [31] likely due to its more intricate topology. Among various structures such as the Gyroid and Lidi-

noid, the SplitP was found to exhibit the best thermal performance based on numerical investigations, as discussed in Ref. [32]. The samples were produced using additive manufacturing technology and subsequently tested at IMDEA Energy Institute using a high-flux solar simulator. Their performance was evaluated and compared based on parameters including temperature increase on the backside surface, outlet temperature, heat absorption, heat loss, and thermal and exergetic efficiencies.

The paper is structured as follows: Section 2.1 offers insights into TPMS lattices, detailing their production and geometry. In Section 2.2, the experimental setup, test facility, and instrumentation employed are introduced. Section 2.3 outlines the procedure followed during the tests. The correlations utilized in data analysis are presented in Section 2.4, while Section 2.5 provides an analysis of uncertainty. Section 3 presents the analyzed results, and Section 4 summarizes the main conclusions.

2. Samples and test campaign

2.1. Planar solar receiver modified with TPMS

The two planar CSP receivers, featuring the described TPMS lattices, were initially designed using nTop and SolidWorks software. Subsequently, they were fabricated using additive manufacturing with the powder bed fusion method, employing Stainless Steel AISI 316L.

TPMS are surfaces with zero mean curvature at each point [33], which minimizes the surface area between the given boundaries [34], providing a high surface-area-to-volume ratio. TPMS structures are developed by periodically repeating a unit cell in three principal directions. These structures could be described by analytical equations composed of sine and cosine functions, shown in Table 1, where $X = 2a\pi x$, $Y = 2b\pi y$, $Z = 2c\pi z$, and a, b and c are constants in charge of the unit cell size of the structures in the x, y and z directions, respectively, while ψ is an offset parameter related to the porosity. - For the mock-ups, the two TPMS selected were Diamond and SplitP, both in sheet form, featuring two parallel channels within each structure. These TPMS were designed with a unit cell size of 10 mm ($a = b = c = 10mm$) and an average wall thickness of 1 mm.

The design porosity, surface-area-to-volume ratio and mass of the samples are reported in Table 2. It should be mentioned that the produced samples were not covered by any coating. The sketch of the receivers with quotes is reported in Fig. 1a–c, while two longitu-

Table 1
Characteristic equations for Diamond and SplitP TPMS lattices.

Structure name	Characteristic function
Diamond	$\sin(X) \cdot \sin(Y) \cdot \sin(Z) + \sin(X) \cdot \cos(Y) \cdot \cos(Z) + \cos(X) \cdot \sin(Y) \cdot \cos(Z) + \cos(X) \cdot \cos(Y) \cdot \sin(Z) = \psi$
SplitP	$1.1 \cdot (\sin(2X) \cdot \sin(Z) \cdot \cos(Y) + \sin(2Y) \cdot \sin(X) \cdot \cos(Z) + \sin(2Z) \cdot \sin(Y) \cdot \cos(X))$ $- 0.2 \cdot (\cos(2X) \cdot \cos(2Y) + \cos(2Y) \cdot \cos(2Z) + \cos(2Z) \cdot \cos(2X))$ $- 0.4 \cdot (\cos(2X) + \cos(2Y) + \cos(2Z)) = \psi$

Table 2
Design values of the porosity, the surface-area-to-volume ratio and mass of the samples.

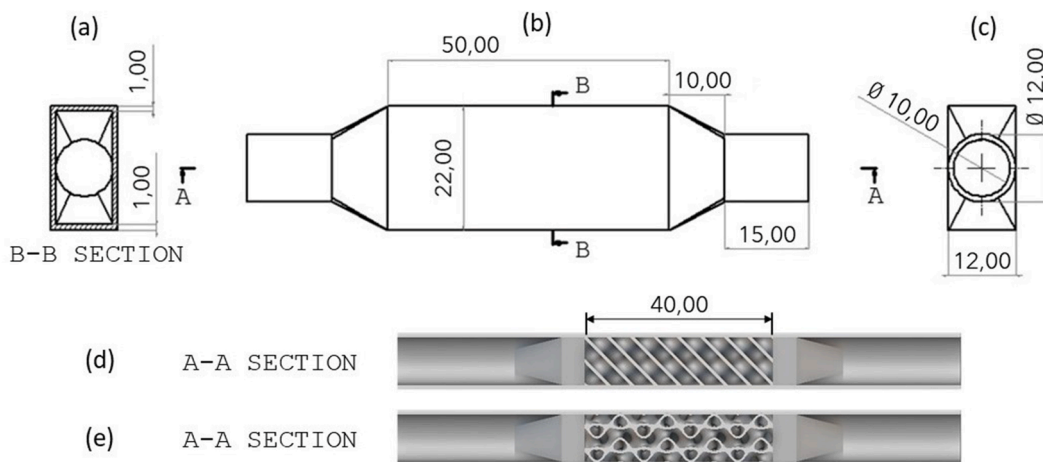|	Diamond	SplitP
Porosity	76.8 %	73.7 %
Surface-area-to-volume ratio [mm^{-1}]	1.06	1.43
Mass [g]	56.5	58.4

Fig. 1. Design Plan of the samples (dimensions are in millimeter) and the 3D CAD of longitudinal cross-section view of the receiver with (d) Diamond lattice and (e) SplitP lattice.

dinal sections on the middle plane, showing the inner TPMS lattices, are shown in Fig. 1d–e. Fig. 2 shows the pictures of the manufactured samples, with an insight view of the lattices. As shown in Fig. 2, the samples exhibit high surface roughness, which leads to increased pressure drop and is expected to give higher heat transfer compared to smooth surfaces. This roughness, intrinsic in the 3D printing process, is challenging to eliminate, and is currently being addressed by dedicated experimental topology investigations.

2.2. Experimental setup

The two samples were tested in the KIRAN-42 high-flux solar simulator, equipped with seven Xenon short-arc lamps (doped tungsten electrodes) with elliptical reflectors placed in a hexagonal symmetry arrangement (Fig. 3a). The emission spectra of KIRAN-42 closely resemble sunlight, and at its maximum capacity (with all seven lamps operating), it delivers a total radiation power of 14 kW with a peak heat flux of 3.6 MW/m^2 at its focal plane [35]. A fully automated XYZ positioning table with an accuracy of 1 mm accommodates the testbed. The latter is exposed to Xenon lamps from a large-aperture window equipped with a blind shutter (Fig. 3b), and another large window (perpendicular to the direction of the heat flux) faces the control room for observation and control. As the tested heat flux range did not exceed 350 kW/m^2, only one lamp (the one in the centre of the hexagonal arrangement) was utilized during the test campaign.

To study the thermal behavior of the planar solar receivers with TPMS lattices, the open loop circuit shown in Fig. 4 was used. Synthetic air, with a composition of 79 % Nitrogen and 21 % Oxygen, supplied from a compressed air bottle, flowed through a pressure regulator valve, maintaining the inlet pressure at approximately 10 bar. Inlet and outlet temperatures, along with absolute pressures, were measured before and after the sample. Notably, due to negligible pressure drops across the samples (below the uncertainty of the pressure gauge), hydraulic measurements are not included in this study. To control the ambient temperature of the test room, the heated air was cooled down in a heat exchanger in a secondary loop with the aid of a chiller, and then exhausted. The temperature of the backside and the downside of the samples were measured using four thermocouples. The locations of the thermocouples on the mounted sample are shown in Fig. 4a. As shown in Fig. 4b a holder was designed and used to hold and ensure the contact between the bottom-side thermocouples and the sample edge. The sensor dimensions and locations were selected to measure varying solid temperatures based on fluid movement within the sample. Two sensors were mounted on the back to measure the heat reaching the outer surface of the samples. Sensor TC_1 was positioned near the fluid entrance, where the air heats up at the maximum rate as it flows through the TPMS channels. Sensor TC_3 was located near the fluid outlet, where the heat transfer rate between the solid and fluid decreases due to a lower temperature gradient. Despite aiming to position the two samples at the same vertical height, a small deviation of 4 mm occurred due to test rig limitations and testing conditions. Additionally, two more thermocouples (TC_2 and TC_4) were in-
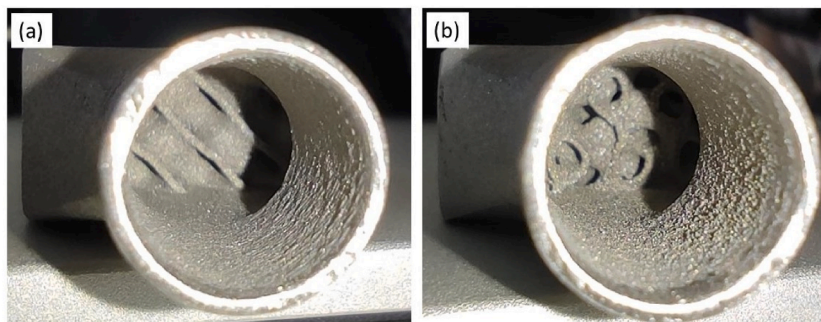

Fig. 2. Pictures of the manufactured samples with (a) Diamond lattice and (b) SplitP lattice.
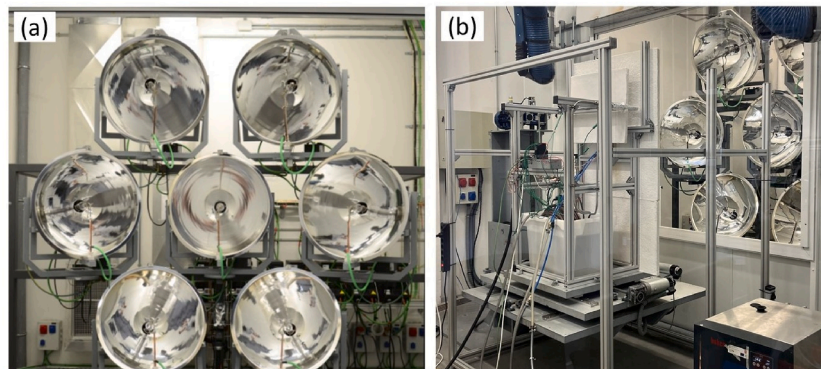

Fig. 3. *(a) Hexagonal arrangement of Xenon lamps (from* Ref. [36]*) (b) The test table.*
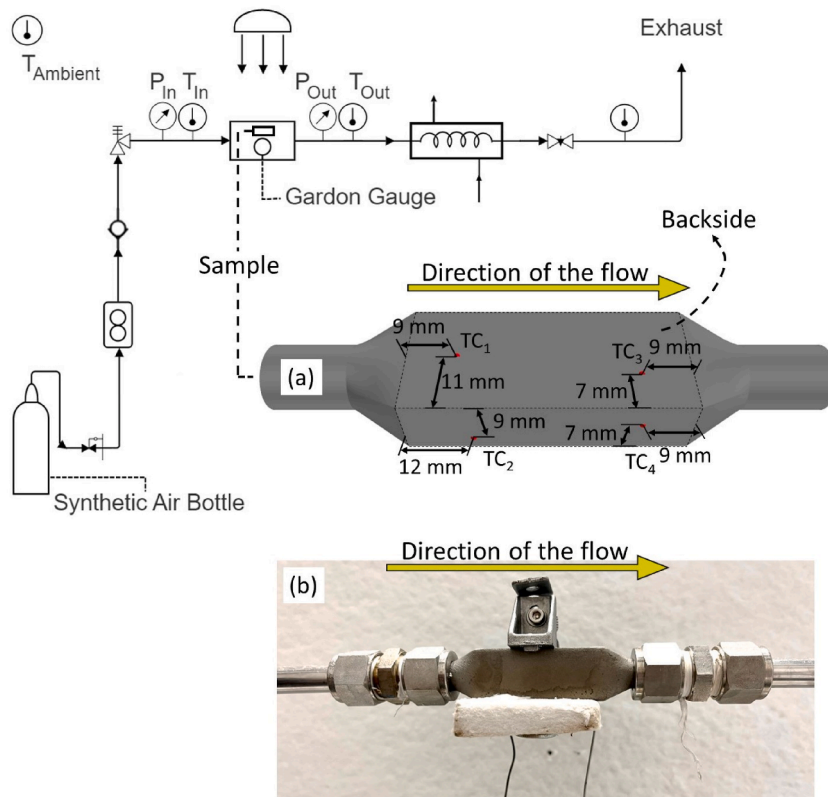
Fig. 4. Sketch of the experimental test setup with (a) Locations of the thermocouples on the backside of the samples (the depth is measured from the back side of the sample) and (b) front side of mounted sample.

stalled on the bottom edge, almost at the same horizontal positions as TC_1 and TC_3, to map the temperature distribution along the sample surfaces and provide insights into hotspot locations along the edges rather than the front side.

It is important to note that temperature readings were conducted using four thermocouples; however, the comparison of temperatures between the two samples relies solely on TC_3, which records readings from the backside. This decision was made due to the inability to securely position the thermocouples TC_2 and TC_4 on the bottom side of the samples, despite the aforementioned holder. As a result, their positions were slightly altered after installation, rendering them incomparable between the two samples.

The instrumentation used to conduct this study includes:

- The temperature sensors, K-type thermocouples manufactured by TC Direct company with an accuracy of ± 0.5 °C with the limit of more than 1000 °C. In the tests, eight thermocouples were used: four thermocouples on the sample, two for the inlet and outlet temperatures, one for the ambient temperature and one for the exhaust air temperature.
- An EL-FlOW F–1170K-MBD-44-V mass flow meter, produced by Bronkhorst and installed upstream of the sample. The accuracy of the mass flow meter was ± 0.1 % in full scale and ± 0.5 % in reading with the maximum capacity of 2 g/s at 20 bar and 20 °C.
- A Thermogage circular-foil heat flux transducer, commonly referred to as a Gardon gauge, specifically the TG1000-1 model manufactured by Vatell. It has a range of 0–160 W/cm^2 and an emissivity of 0.95. While the nominal accuracy is stated as ± 3 %, the operator at IMDEA Energy Institute recommended a tolerance of ± 10 %.
- Two 0–10 V DC output pressure transmitters made by TC Direct, installed upstream and downstream of the sample, respectively, with the accuracy of ± 0.5 % in full scale, the range of 0–16 bar and output of 0–10 V. However, since the pressure drop along the sample was very low, these measurements were not analyzed as the accuracy of the uncertainty of the pressure drop resulted to be of the same order of the measured pressure difference between inlet and outlet.

All the data from the sensors were recorded at the same time with the frequency of 2 s.

2.3. Experimental procedure

The test campaign was carried out from November 7th to November 17th, 2023 at IMDEA Energy Institute in Madrid to evaluate the thermal behavior of the two TPMS lattices under different heat fluxes and mass flow rates. The experiments were carried out as part of the international access program within the SFERA-III project funded by the EU. Prior to conducting the tests, preliminary simulations were executed using the commercial CFD software STAR-CCM + [37]. These simulations aimed to establish the experimental test parameters and verify that the hot spot temperatures remained below the softening temperature of Stainless Steel.

The mass flow adjustment was performed at the beginning of each test session, with each test performed for constant mass flow rate and different heat flux levels. Subsequently, the Xenon lamp located at the center of the hexagonal arrangement in Fig. 3a was activated for a duration of 10 min to ensure a stable flux. To prevent lamp overheating, a continuous blower operation was employed throughout the tests. During this phase, precautions were taken to safeguard the sample from damage; the test table was positioned vertically so that the concentrated power was directed at the Lambertian target rather than the sample. The solar simulator's focal plane exhibits a Gaussian distribution of heat flux originating from the Xenon lamp, as depicted in Fig. 5. Consequently, to achieve diverse heat flux levels on the absorbing surface, the samples were positioned at different locations on the flux map to achieve the corresponding average value. To achieve the desired heat flux, the Gardon gauge sensor was placed at the sample location on the Lambertian target. After positioning the target on the lamp's concentrator focal plane, the testbed was vertically adjusted to record the corresponding coordinates for the desired heat flux. This procedure was recommended by the IMDEA Energy Institute's personnel and it is reported in Ref. [38]. After the primary adjustments, the bottle's valve was reopened, and the table was placed at the vertical location corresponding to the desired heat flux level.

The tests for the Diamond lattice were completed before the installation of the SplitP sample. Each test aimed to achieve a quasi-steady state condition, allowing approximately 10 min for data recording once this condition was reached before concluding the test. Test names were derived from the first character of the TPMS lattice, followed by the heat flux level and mass flow rate. For instance, "D100-20″ denotes a test conducted on the Diamond sample with a heat flux level of 100 kW/m^2 and a mass flow rate of 2 g/s. Table 3 summarizes the conducted tests and reports the test names and their corresponding mass flow rate and heat flux level.

2.4. Data analysis

Theoretically, the heat flux distribution in the solar simulator exhibits rotational symmetry, with the maximum value at the center [39]. On the initial testing day, following the procedure outlined in Section 2.3, vertical locations on the focal plane corresponding to desired heat flux levels were documented. However, since the heat flux varies across the receiver's surface, a correlation was established between the recorded vertical locations and their associated heat flux values. Utilizing ten coordinates and their respective measured heat flux values, Eq. (1) was derived to model the Gaussian heat flux distribution:

$$HF = A + He^{-0.5\left[\left(\frac{x}{\sigma_x}\right)^2 + \left(\frac{y}{\sigma_y}\right)^2\right]} \tag{1}$$

In Eq. 1, A = 94.43 kW/m^2, H = 245.08 kW/m^2 and $\sigma_x = \sigma_y = 15.575$ are the standard deviations in x and y directions, obtained as the best fit of the ten measured heat flux values and their corresponding locations. In Fig. 5, the heat flux distribution from Eq. (1) is shown, and the vertical locations of the sample for the heat flux levels of 100 and 300 kW/m^2 are highlighted ((a) and (b), respectively). The vertical locations of the studied heat flux levels and their corresponding incident heat (obtained from Eq. (1)) are reported in Table 4. The origin of the coordinate system corresponds to the maximum value of heat flux on the focal plane. The total incident heat, E_{tot}, is obtained by integrating Eq. (1) on the receiver:

$$E_{tot} = \iint \left[A + He^{-0.5\left[\left(\frac{x}{\sigma_x}\right)^2 + \left(\frac{y}{\sigma_y}\right)^2\right]}\right] dxdy \tag{2}$$
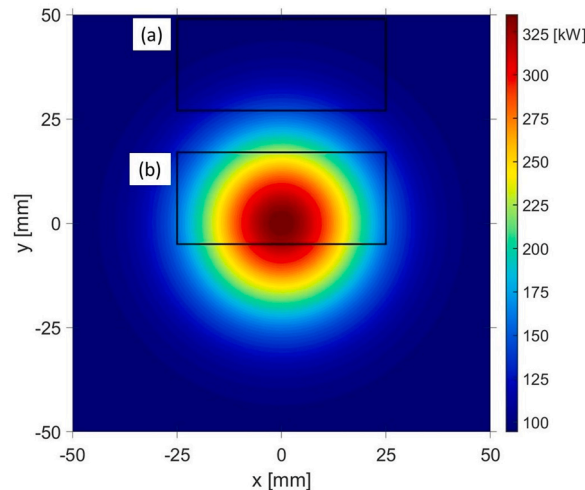

Fig. 5. Heat flux distribution based on Eq. (1), and the location of the sample for a heat flux level of (a) 100 kW/m^2 and (b) 325 kW/m.^{2}.

Table 3
Tests information containing the test names and their corresponding mass flow rate and heat flux level.

Sample	Mass flow rate (g/s)	Heat flux level (kW/m^2)	Test name	Sample	Mass flow rate (g/s)	Heat flux level (kW/m^2)	Test name
Diamond	0.5	100	D100-05	**SplitP**	0.5	100	S100-05
		125	D125-05			125	S125-05
		150	D150-05			150	S150-05
		200	D200-05			200	S200-05
	1	100	D100-10		1	100	S100-10
		125	D125-10			125	S125-10
		150	D150-10			150	S150-10
		200	D200-10			200	S200-10
		250	D250-10			250	S250-10
		300	D300-10			300	S300-10
	1.5	100	D100-15			325	S325-10
		125	D125-15		1.5	100	S100-15
		150	D150-15			125	S125-15
		200	D200-15			150	S150-15
		250	D250-15			200	S200-15
		300	D300-15			250	S250-15
		325	D325-15			300	S300-15
	2	100	D100-20			325	S325-15
		125	D125-20		2	100	S100-20
		150	D150-20			125	S125-20
		200	D200-20			150	S150-20
		250	D250-20			200	S200-20
		300	D300-20			250	S250-20
		325	D325-20			300	S300-20
						325	S325-20

Table 4
Vertical locations (origin at x = 0 and y = 0) associated to each heat flux level and the incident heat from Eq.

Nominal heat flux level [kW/m^2]	Δy[a] [mm]	Incident heat E_{tot} [W]
100	38	117.4 ± 11.7
125	33	129.4 ± 12.9
150	28	147.6 ± 14.8
200	20	189.9 ± 19.0
250	14	226.9 ± 22.7
300	9	254.2 ± 25.4
325	6	266.5 ± 26.7

[a] Vertical location of the test bed.

Unfortunately, not all the incident solar energy is absorbed and transferred to the flow. The amount of absorbed heat is dependent on the optical efficiency of the concentrator, absorptivity of the receiver and also the amount of heat loss to the ambient through radiation and convective heat losses. The absorbed heat is calculated from Eq. (3), assuming quasi-steady state conditions.

$$E_u = \dot{m} c_p \left(T_o - T_i \right) \tag{3}$$

In Eq. (3), $\dot{m}$ is the mass flow rate, T_i and T_o are the inlet and outlet average temperatures of the fluid, respectively and c_p is the specific heat of synthetic air (obtained at $(T_i + T_o)/2$). The amount of heat loss is the difference between the incident heat E_{tot} and the absorbed heat E_u (Eq. (4)).

$$E_{loss} = E_{tot} - E_u \tag{4}$$

The thermal efficiency of the receiver, defined as the ratio between the absorbed heat and the total incident heat, is calculated from Eq. (5):

$$\eta_{th} = \frac{E_u}{E_{tot}} \tag{5}$$

The exergy efficiency is defined as Eq. (6):

$$\eta_{ex} = \frac{Ex_u}{Ex_{tot}} \tag{6}$$

which is the ratio between the absorbed exergy rate (Eq. (7)) and the exergy of incident concentrated solar power (Eq. (8)).

$$Ex_u = E_u - \dot{m} C_p T_{amb} \, ln \left(\frac{T_o}{T_i} \right) = \dot{m} C_p \left[(T_o - T_i) - T_{amb} \, ln \left(\frac{T_o}{T_i} \right) \right] \tag{7}$$

The total exergy from the incident radiation concentrated on the sample, Ex_{tot}, was calculated using the correlation introduced by Petela [40].

$$Ex_{tot} = E_{tot} \left[1 + \frac{1}{3} \left(\frac{T_{amb}}{T_{sun}} \right)^4 - \frac{4 T_{amb}}{3 T_{sun}} \right] \tag{8}$$

In Eq. (8), the temperature of the heat source (Xenon lamp) was assumed to be equal to the temperature of the sun, T_{sun}, and equal to 5762 K.

2.5. Analysis of experimental uncertainty

Each measuring instrument operates within a specified range and possesses a certain level of uncertainty. When calculating parameters derived from measured quantities, it is common practice to consider the instrumentation's uncertainty as an independent variable. For example, the dependent function R is related to independent variables $\omega_1, \omega_2, \omega_3, \ldots, \omega_n$ through Eq. (9).

$$R = R (\omega_1, \omega_2, \omega_3, \ldots, \omega_n) \tag{9}$$

According to Holman [41], the uncertainty of a dependent variable R, W_R, can be calculated as in Eq. (10):

$$W_R = \left[\left(\frac{\partial R}{\partial \omega_1} W_1 \right)^2 + \left(\frac{\partial R}{\partial \omega_2} W_2 \right)^2 + \ldots + \left(\frac{\partial R}{\partial \omega_n} W_n \right)^2 \right]^{\frac{1}{2}} \tag{10}$$

In which, W_1, W_2, ..., W_n are the uncertainty of independent variables $\omega_1, \omega_2, \ldots, \omega_n$.

The uncertainty of absorbed heat, energy and exergy efficiencies is then calculated as reported in Eqs. (11)–(14):

$$W_{E_u} = \left[\left(\frac{\partial E_u}{\partial \dot{m}} W_{\dot{m}} \right)^2 + \left(\frac{\partial E_u}{\partial T_{out}} W_{T_{out}} \right)^2 + \left(\frac{\partial E_u}{\partial T_{in}} W_{T_{in}} \right)^2 \right]^{\frac{1}{2}} \tag{11}$$

$$W_{\eta_{th}} = \left[\left(\frac{\partial \eta_{en}}{\partial E_{tot}} W_{E_{tot}} \right)^2 + \left(\frac{\partial \eta_{en}}{\partial \dot{m}} W_{\dot{m}} \right)^2 + \left(\frac{\partial \eta_{en}}{\partial T_{in}} W_{T_{in}} \right)^2 + \left(\frac{\partial \eta_{en}}{\partial T_{out}} W_{T_{out}} \right)^2 \right]^{\frac{1}{2}} \tag{12}$$

$$W_{\eta_{ex}} = \left[\left(\frac{\partial \eta_{ex}}{\partial Ex_{tot}} W_{Ex_{tot}} \right)^2 + \left(\frac{\partial \eta_{ex}}{\partial \dot{m}} W_{\dot{m}} \right)^2 + \left(\frac{\partial \eta_{ex}}{\partial T_{in}} W_{T_{in}} \right)^2 + \left(\frac{\partial \eta_{ex}}{\partial T_{out}} W_{T_{out}} \right)^2 + \left(\frac{\partial \eta_{ex}}{\partial T_{amb}} W_{T_{amb}} \right)^2 \right]^{\frac{1}{2}} \tag{13}$$

where:

$$W_{Ex_{tot}} = \left[\left(\frac{\partial Ex_{tot}}{\partial E_{tot}} W_{E_{tot}} \right)^2 + \left(\frac{\partial Ex_{tot}}{\partial T_{amb}} W_{T_{amb}} \right)^2 \right]^{\frac{1}{2}} \tag{14}$$

All temperatures in theses relations were offset to their initial value; therefore, the difference between T_{in} and T_{out} before applying the heat flux was excluded from the calculations. The details of experimental errors are provided in Table 5.

Table 5
Experimental error sources and their relative uncertainty.

Variable	Uncertainty	Value
Concentrated flux	E_{tot}	±10 %
Air flow rate	$W_{\dot{m}}$	±1.5 %
Temperature	W_T, $W_{T_{out}}$, $W_{T_{amb}}$, W_{TC_1}, W_{TC_2}, W_{TC_3}, W_{TC_4}	±1.5 °C
Absorbed heat	W_{E_u}	±1.9 %
Heat loss	$W_{E_{loss}}$	±22 %
Thermal efficiency	$W_{\eta_{th}}$	±10.2 %
Exergy efficiency	$W_{\eta_{ex}}$	±11 %

3. Results and discussion

During the postprocessing of the results, the uncertainty associated with each independent variable was determined by summing the standard deviation of the extracted results and the uncertainty inherent in the respective measuring tool.

The Reynolds number is introduced in Eq. (15) (where ρ and μ are the fluid density and dynamic viscosity, respectively, evaluated at the average fluid temperature, and U_s is the average superficial fluid velocity), defined based on a hydraulic diameter D_h:

$$Re = \frac{\rho U_s D_h}{\mu} \tag{15}$$

In TPMS lattices, D_h is defined as in Eq. (16):

$$D_h = \frac{4V_{fluid}}{A_{wet}} \tag{16}$$

where, V_{fluid} is the fluid volume and A_{wet} is the wetted surface. The pore velocity U_s, is calculated from Eq. (17), where A_c is the cross-sectional area of the receiver.

$$U_s = \frac{\dot{m}D_h}{A_c \varepsilon \rho} \tag{17}$$

Upon reviewing existing literature, it becomes evident that only a limited number of studies have delved into the transition to turbulent flow, highlighting the necessity for further investigation on this topic. Iyer et al. [34] explored laminar flow through TPMS structures, considering Reynolds numbers up to approximately 300 to be within the laminar regime. It is noteworthy that, unlike the scenario observed in smooth pipes, the transition to turbulent flow is gradual, with no drastic changes in the friction factor [42]. Table 6 presents the Reynolds numbers corresponding to each sample within the examined range of mass flow rates. For a mass flow rate of 0.5 g/s, the Reynolds number appears to lie within the transitional region, whereas for a mass flow rate of 1 g/s, it is reasonable to assume that the flow has transitioned to the turbulent regime.

3.1. Temperature profile

An illustration of the measured results, including the transient period for a test session with a mass flow rate of 0.5 g/s for the sample featuring the SplitP lattice, is provided in Fig. 6. It is worth noting that the sample with the Diamond lattice exhibits a similar behavior to that of the SplitP lattice; hence, it is not depicted in Fig. 6. The quasi-steady state results were recorded for approximately 10 min before proceeding to the next heat flux level. To mitigate potential issues stemming from imperfect thermocouple calibration,

Table 6
Reynolds number of the tests.

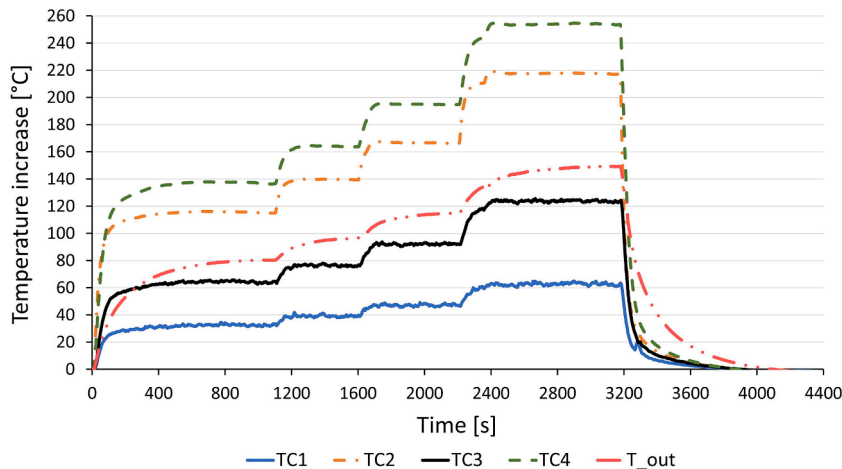| Mass flow rate (g/s)	Reynolds number	
	SplitP lattice	Diamond lattice
0.5	430	530
1	860	1000
2	1700	2100

Fig. 6. An example of a test session with the mass flow rate of 0.5 g/s for sample with SplitP lattice. The temperature increase is referred to room temperature.

each signal was offset to its initial value, ensuring a starting measurement of zero for each parameter. Since the ambient temperature was nearly constant (in the range of 19–22 °C), it was not shown in Fig. 6; however, for each test, its value was obtained with the aforementioned method.

Fig. 6 illustrates the transient cooling phase, characterized by a rapid spike in temperature readings. The time needed for the temperatures measured by TC$_3$ to cool down from 130 °C to 98 % of the ambient temperature was 14 % higher for the Diamond sample. This suggests a faster transient response in the SplitP sample, likely due to its higher effective thermal diffusivity. According to simple dimensional analysis on the transient heat diffusion equation, the transient timescale scales inversely with thermal diffusivity. While an exact calculation of thermal diffusivity requires additional information about the mean temperature of the samples, the assumption of higher effective thermal diffusivity in the SplitP sample is acceptable, given its smaller porosity and higher mass compared to the Diamond sample (refer to Table 2).

In their insightful exploration of the thermal conductivity of TPMS lattice structures, Catchpole-Smith et al. [43] deduced that the thermal conductivity is primarily determined by the solid volume fraction, defined as the ratio of solid material volume to the void volume (V_{Solid}/V_{Fluid}). Put differently, the effective conductivity of the lattice is inversely related to the porosity $\varepsilon = V_{Fluid}/(V_{Fluid} + V_{Solid}) = 1/(1 + V_{Solid}/V_{Fluid})$. They attributed this phenomenon to the increase in wall thickness. Additionally, thermal conductivity is influenced by geometry, unit cell size, and the surface roughness of 3D printing. SplitP, in comparison to the Diamond lattice, exhibits a lower porosity and higher mass (refer to Table 2). Consequently, this results in a higher effective conductivity, thereby promoting conduction heat transfer from the heated surface to the back side of the sample.

The temperature increases (relative to initial temperatures) of the backside temperature TC$_3$ and the outlet temperatures of the samples are illustrated in Fig. 7. All measured temperatures for the SplitP sample exhibit higher values compared to Diamond. In Fig. 7 (a) and (b), the SplitP sample shows a higher outlet temperature increase compared to the Diamond sample. This difference suggests that the SplitP lattice absorbs more heat overall with lower heat loss, validating the higher temperature readings by TC$_3$ in the SplitP sample, as shown in Fig. 7 (c) and (d).

In Fig. 8, the temperature increases (compared to room temperature) of all four thermocouples mounted on the samples and of the outlet temperature is shown for the mass flow rates of 0.5 and 2 g/s and the highest incident heat flux levels tested for those mass flow rates. For both samples, the temperature measured by the different thermocouples increases, as expected, along the samples in the direction of the fluid flow. Notably, temperatures measured at the back face of the samples (TC$_3$) are consistently lower than those recorded on their sides (TC$_2$ and TC$_4$), attributable to the latter sensors' closer proximity to the heated surface. It is noteworthy that temperatures measured on the SplitP lattice sample consistently exceed those of the Diamond lattice sample. However, it is essential to highlight that direct comparisons between TC$_2$ and TC$_4$ measurements for the two samples may not be entirely accurate, as discussed in Section 2.2.

3.2. Absorbed heat

The absorbed heat computed for each sample is shown in Fig. 9 for different values of the mass flow rate. As expected, the absorbed heat increases with higher mass flow rates and higher incident heat fluxes. As the heat flux increases, the absorbed heat progressively deviates more from the ideal condition ($E_u = E_{tot}$) which is the bisecting line of the graph and is plotted with a black dashed line. This effect is due to the higher temperature levels reached by the samples for higher incident heat rates and thus to a higher heat
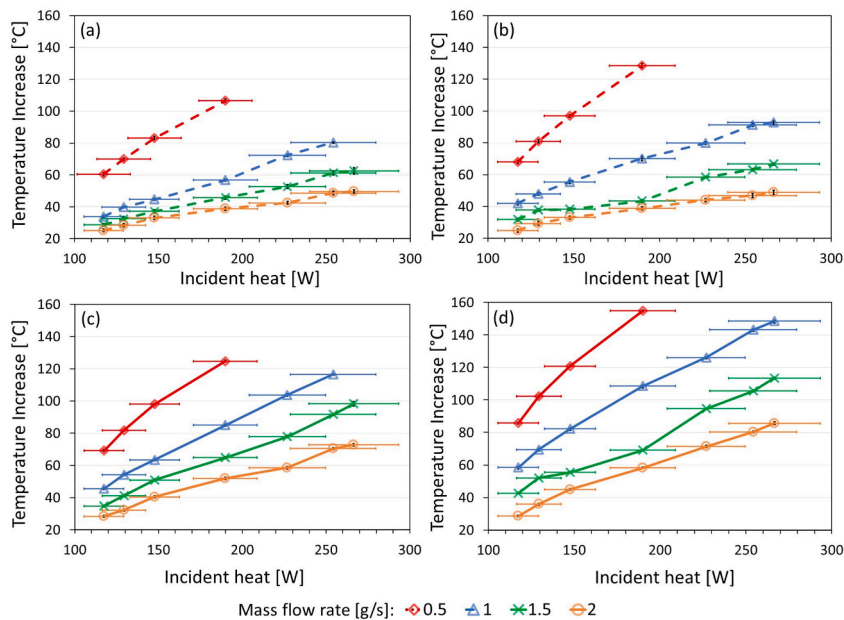

Fig. 7. Temperature rise with respect to room temperature at the outlet (a,c) and in TC3 (b,d) for Diamond (a,c) and SplitP (b,d).
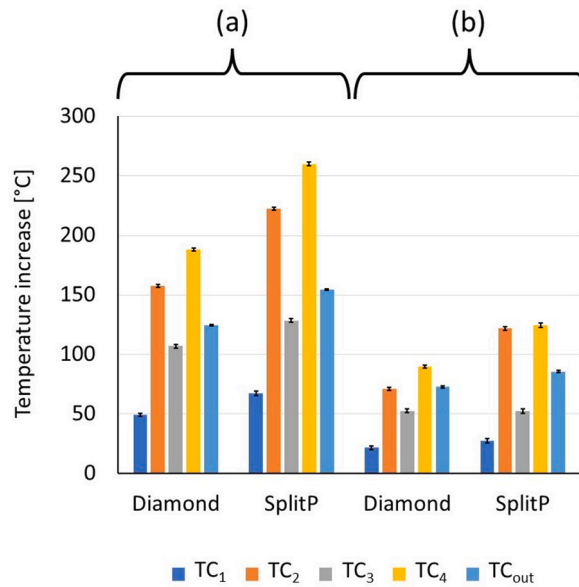
Fig. 8. Temperature increase (with respect to room temperature) of the four thermocouplses on the samples for (a) mass flow rate of 0.5 and incident heat of 200 W and (b) mass flow rate of 1 g/s and the incident heat of 270 W.
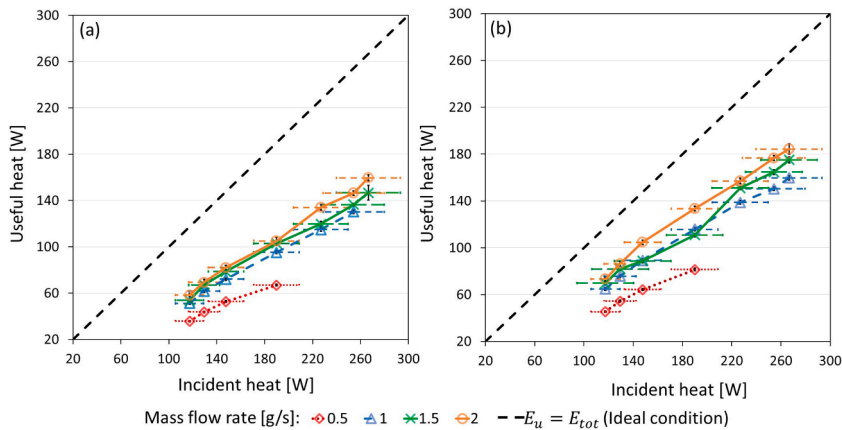

Fig. 9. Absorbed heat absorbed by the samples for different incident heat for (a) Diamond and (b) SplitP samples.

losses to the ambient. Across all mass flow rates and incident heat levels, the SplitP lattice sample demonstrates enhanced heat removal compared to the Diamond lattice counterpart.

3.3. Heat loss and efficiency

The total heat loss from the receivers was calculated from Eq. (4) and could be seen in Fig. 10a–b, and it turned out to be a very significant fraction of the incident heat, ranging from 30 % in the most favourable case (SplitP lattice with the highest flow rate and the highest incident heat) to 70 % in the worst case (Diamond lattice with the lowest mass flow rate and lowest incident heat). As anticipated, increasing the mass flow rate leads to a decrease in heat loss for each sample, as more effective cooling occurs, limiting the temperature rise of the receiver for a given incident heat value. The rise in incident heat from the minimum to maximum value marginally reduces the loss ratio: as heat flux increases, the proportion of heat lost relative to the incident heat decreases for both samples across all tested air flow rates. This suggests that with higher heat fluxes, a greater portion of the incident heat is absorbed, corroborating the findings in Fig. 9. The SplitP lattice sample shows a lower loss ratio, attributed to its higher absorption of incident heat. It is crucial to highlight that temperature readings were not taken on the heated surface of the samples, as previously discussed in Section 2.2.

To assess the thermal performance of each design across various heat flux levels and mass flow rates, thermal efficiency (as per Eq. (5)) was computed and compared in Fig. 10c–d. In both cases, thermal efficiency increases with higher mass flow rates, tending to stabilize at the highest flow rate values. Once again, the SplitP sample exhibits superior performance. The highest thermal efficiency is achieved with a mass flow rate of 2 g/s, reaching approximately 70 % for SplitP and nearly 60 % for the Diamond. Table 7 provides a
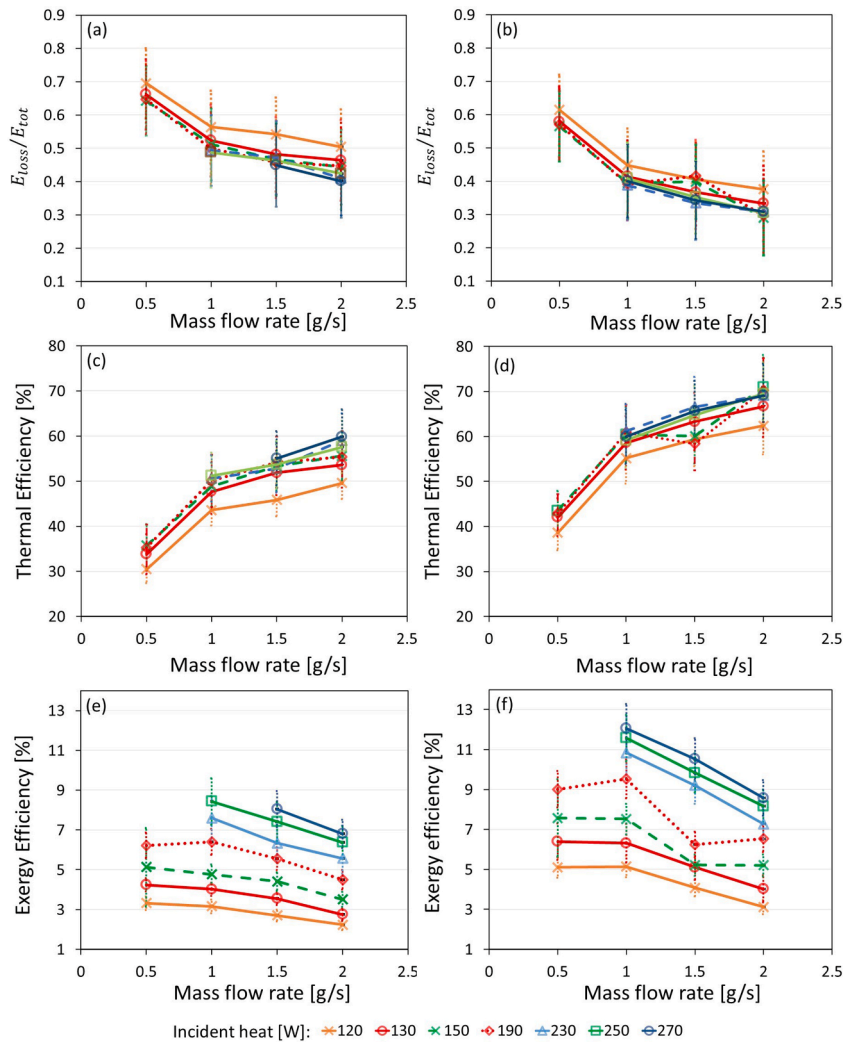
Fig. 10. Normalized heat loss, thermal efficiency and exergetic efficiency for (a) Diamond and (b) SplitP samples.

Table 7
Thermal efficiencies of different solar air heaters, in a mass flow rate range relevant to the present study.

Solar air heater	Maximum η_{th} (%)	Flow rate of air
CPC[a] [44]	~50 %	0.0019–0.002 [m³/s]
PTC with internal fins [45]	~45 %	0.0016–0.0086 [m³/s]
Conical concentrator [46]	~20 %	8.3 g/s
FPC[b] with CPC [47]	~30 %	2.2 g/s
Double-pass unglazed FPC with perforated absorber plate and packing wire mesh layers [48]	~15 %	3 g/s
FPC [49]	~35 %	4 g/s

[a] Compound parabolic concentrator.
[b] Flat plate collector.

comparison of thermal efficiencies for various solar air heaters within a mass flow rate range similar to this study. It is evident that even at higher flow rates, the thermal efficiencies obtained are lower than those observed in the tested receivers with TPMS lattices.

The values of exergy efficiency (Eq. (6)) for the samples in all tests are reported in Fig. 10e–f. Still SplitP has a higher exergetic efficiency compared to Diamond. The highest values of exergy efficiency in the tests were observed for the mass flow rate of 1 g/s and it was around 12 % for SplitP at the incident heat of ~270 W, while it was nearly 8.5 % for Diamond at the incident heat of ~250 W. The lowest value of the exergetic efficiency was found for both samples at the highest flow rate and lowest incident heat. For each mass flow rate, an increase is observed in exergy efficiency with increasing heat fluxes; however, this is not the case with the increase in the mass flow rate. Reviewing the literature reveals that solar air heaters featuring various roughness geometries typically exhibit a

maximum exergy efficiency of less than 1.5 % for equivalent Reynolds numbers [49–51]. Similarly, in the context of concentrated solar power with porous inserts, the reported maximum exergy efficiency for various Raschig Ring inserts remained below 5 % at a heat flux of 200 kW/m^2 [39].

4. Conclusions and perspective

This experimental work assesses the effects of using TPMS lattices (namely, Diamond and SplitP) as porous media for high temperature CSP applications. Two Stainless Steel planar receivers equipped with SplitP, and Diamond lattices were designed, produced by additive manufacturing and studied in an experimental campaign at the IMDEA Energy Institute. Their thermal performance was studied under four different mass flow rate values and seven levels of incident heat flux with synthetic air as the working fluid. The main findings in this study are the following:

- The maximum thermal efficiency obtained in the tests occurred at the maximum mass flow rate of 2 g/s and was around 70 % for the SpitP sample, while it was approximately 60 % for the Diamond sample. This finding holds significant importance, particularly considering that the Diamond lattice was previously regarded as the superior choice among various TPMS options by several researchers, excluding the SplitP lattice.
- The highest exergetic efficiency in the tests was observed at the mass flow rate of 1 g/s and was approximately 12 % for SplitP at ~270 W, and 8.5 % for Diamond at ~250 W.
- As the mass flow rate increases, the E_{loss}/E_{tot} ratio decreases as the HTF absorbs a larger fraction of the incident heat.
- The sample with the SplitP lattice showed superior thermal performance with larger absorbed heat and lower heat losses with respect to the Diamond sample. The plausible explanation for that lays in the lower temperature on the heated surface, but this should be verified by appropriate numerical modeling as the heated surface temperature was not measured directly.

Looking ahead, the experimental findings will undergo thorough analysis through CFD simulations. These simulations will involve selecting the most appropriate turbulence closure method to accurately replicate the measured temperatures. Additionally, they will offer valuable insights, including the determination of hot spot temperatures on the heated surfaces. Concurrently, another test campaign is scheduled to focus on measuring the hydraulic characteristics of the two samples, which will facilitate the finalization of the comparison between the two TPMS lattices.

CRediT authorship contribution statement

A. Mortazavi: Writing – original draft, Visualization, Methodology, Investigation, Formal analysis, Data curation. **A.L. Ávila-Marín:** Writing – review & editing. **H. Ebadi:** Writing – original draft, Visualization, Methodology, Investigation, Formal analysis, Data curation. **E. Gajetti:** Writing – review & editing, Visualization, Methodology, Investigation, Formal analysis, Data curation. **C. Piatti:** Writing – review & editing, Methodology, Investigation, Formal analysis, Data curation. **L. Marocco:** Writing – review & editing, Supervision, Methodology, Funding acquisition, Conceptualization. **L. Savoldi:** Writing – review & editing, Supervision, Resources, Methodology, Conceptualization.

Declaration of competing interest

The authors declare the following financial interests/personal relationships which may be considered as potential competing interests:Arsham Mortazavi, Eleonora Gajetti, Hossein Ebadi, Cecilia Piatti reports travel was provided by European Union. If there are other authors, they declare that they have no known competing financial interests or personal relationships that could have appeared to influence the work reported in this paper.

Data availability

Data will be made available on request.

Acknowledgment

References

[1] I. Renewable Energy Agency, Renewable Capacity Statistics 2024, 2024.
[2] E. Kabir, P. Kumar, S. Kumar, A.A. Adelodun, K.-H. Kim, Solar energy: potential and future prospects, Renew. Sustain. Energy Rev. 82 (2018) 894–900, https://doi.org/10.1016/j.rser.2017.09.094.
[3] IEA, Technology Roadmap - Concentrating Solar Power, 2010 Paris.
[4] B. Belgasim, Y. Aldali, M.J.R. Abdunnabi, G. Hashem, K. Hossin, The potential of concentrating solar power (CSP) for electricity generation in Libya, Renew. Sustain. Energy Rev. 90 (2018) 1–15, https://doi.org/10.1016/j.rser.2018.03.045.
[5] W. Ding, T. Bauer, Progress in research and development of molten chloride salt technology for next generation concentrated solar power plants, Engineering 7 (2021) 334–347, https://doi.org/10.1016/j.eng.2020.06.027.
[6] E. Bellos, C. Tzivanidis, Investigation of a star flow insert in a parabolic trough solar collector, Appl. Energy 224 (2018) 86–102, https://doi.org/10.1016/j.apenergy.2018.04.099.
[7] E. Bellos, C. Tzivanidis, K.A. Antonopoulos, A detailed working fluid investigation for solar parabolic trough collectors, Appl. Therm. Eng. 114 (2017) 374–386, https://doi.org/10.1016/j.applthermaleng.2016.11.201.

[8] J. Flesch, L. Marocco, A. Fritsch, K. Niedermeier, T. Wetzel, Entropy generation minimization analysis of solar salt, sodium, and lead–bismuth eutectic as high temperature heat transfer fluids, J. Heat Tran. 142 (2020), https://doi.org/10.1115/1.4046302.

[9] Y.-R. Galindo-Luna, H. Sánchez-Mora, G. Espinosa-Paredes, É.-G. Espinosa-Martínez, Performance comparison of PTCs with nanoparticles in water and nanoparticle in thermal oil, Case Stud. Therm. Eng. 50 (2023) 103478, https://doi.org/10.1016/j.csite.2023.103478.

[10] K. Burlafinger, A. Vetter, C.J. Brabec, Maximizing concentrated solar power (CSP) plant overall efficiencies by using spectral selective absorbers at optimal operation temperatures, Sol. Energy 120 (2015) 428–438, https://doi.org/10.1016/j.solener.2015.07.023.

[11] G. Rossi, A. D'Angelo, C. Diletto, S. Esposito, A. Guglielmo, M. Lanchi, New spectrally selective coatings for CSP linear receivers operating in air at high temperature, Appl. Res. 3 (2024) e202200117, https://doi.org/10.1002/appl.202200117.

[12] P. Wang, D.Y. Liu, C. Xu, Numerical study of heat transfer enhancement in the receiver tube of direct steam generation with parabolic trough by inserting metal foams, Appl. Energy 102 (2013) 449–460, https://doi.org/10.1016/j.apenergy.2012.07.026.

[13] A. Mwesigye, T. Bello-Ochende, J.P. Meyer, Heat transfer and thermodynamic performance of a parabolic trough receiver with centrally placed perforated plate inserts, Appl. Energy 136 (2014) 989–1003, https://doi.org/10.1016/j.apenergy.2014.03.037.

[14] M.T. Jamal-Abad, S. Saedodin, M. Aminy, Experimental investigation on a solar parabolic trough collector for absorber tube filled with porous media, Renew. Energy 107 (2017) 156–163, https://doi.org/10.1016/j.renene.2017.02.004.

[15] L. Savoldi, A. Allio, A. Bovento, M. Cantone, J. Fernandez Reche, Experimental and numerical investigation of a porous receiver equipped with Raschig Rings for CSP applications, Sol. Energy 212 (2020) 309–325.

[16] H. Ebadi, A. Cammi, N. Fathi, L. Savoldi, Pore-scale simulation of a tubular solar absorber partially filled with Raschig ring porous medium for efficiency enhancement purposes, in: ASME Power Appl. R&D 2023, ASME, 2023, https://doi.org/10.1115/POWER2023-108768.

[17] H. Ebadi, A. Cammi, E. Gajetti, L. Savoldi, Development, verification and experimental validation of a 3D numerical model for tubular solar receivers equipped with Raschig Ring porous inserts, Sol. Energy 267 (2024) 112236, https://doi.org/10.1016/j.solener.2023.112236.

[18] H.H. Gerke, M.T. van Genuchten, A dual-porosity model for simulating the preferential movement of water and solutes in structured porous media, Water Resour. Res. 29 (1993) 305–319, https://doi.org/10.1029/92WR02339.

[19] J. Tian, T. Kim, T.J. Lu, H.P. Hodson, D.T. Queheillalt, D.J. Sypeck, H.N.G. Wadley, The effects of topology upon fluid-flow and heat-transfer within cellular copper structures, Int. J. Heat Mass Tran. 47 (2004) 3171–3186, https://doi.org/10.1016/j.ijheatmasstransfer.2004.02.010.

[20] J. Tian, T.J. Lu, H.P. Hodson, D.T. Queheillalt, H.N.G. Wadley, Cross flow heat exchange of textile cellular metal core sandwich panels, Int. J. Heat Mass Tran. 50 (2007) 2521–2536, https://doi.org/10.1016/j.ijheatmasstransfer.2006.11.042.

[21] S.-H. Oh, C.-H. An, B. Seo, J. Kim, C.Y. Park, K. Park, Functional morphology change of TPMS structures for design and additive manufacturing of compact heat exchangers, Addit. Manuf. 76 (2023) 103778, https://doi.org/10.1016/j.addma.2023.103778.

[22] G. Yan, M. Sun, Y. Liang, S. Li, Z. Zhang, X. Zhang, Y. Song, Y. Liu, J. Zhao, Simulation and experimental study on flow and heat transfer performance of sheet-network and solid-network disturbance structures based on triply periodic minimal surface, Int. J. Heat Mass Tran. 219 (2024) 124905, https://doi.org/10.1016/j.ijheatmasstransfer.2023.124905.

[23] M.G. Gado, S. Ookawara, H. Hassan, Utilization of triply periodic minimal surfaces for performance enhancement of adsorption cooling systems: computational fluid dynamics analysis, Energy Convers. Manag. 277 (2023) 116657, https://doi.org/10.1016/j.enconman.2023.116657.

[24] W. Tang, H. Zhou, Y. Zeng, M. Yan, C. Jiang, P. Yang, Q. Li, Z. Li, J. Fu, Y. Huang, Y. Zhao, Analysis on the convective heat transfer process and performance evaluation of triply periodic minimal surface (TPMS) based on Diamond, gyroid and iwp, Int. J. Heat Mass Tran. 201 (2023) 123642, https://doi.org/10.1016/j.ijheatmasstransfer.2022.123642.

[25] W. Li, G. Yu, Z. Yu, Bioinspired heat exchangers based on triply periodic minimal surfaces for supercritical CO2 cycles, Appl. Therm. Eng. 179 (2020) 115686, https://doi.org/10.1016/j.applthermaleng.2020.115686.

[26] M. Khalil, M.I. Hassan Ali, K.A. Khan, R. Abu Al-Rub, Forced convection heat transfer in heat sinks with topologies based on triply periodic minimal surfaces, Case Stud. Therm. Eng. 38 (2022) 102313, https://doi.org/10.1016/j.csite.2022.102313.

[27] M. Modrek, A. Viswanath, K.A. Khan, M.I.H. Ali, R.K. Abu Al-Rub, An optimization case study to design additively manufacturable porous heat sinks based on triply periodic minimal surface (TPMS) lattices, Case Stud. Therm. Eng. 36 (2022) 102161, https://doi.org/10.1016/j.csite.2022.102161.

[28] G. Yan, M. Sun, Z. Zhang, Y. Liang, N. Jiang, X. Pang, Y. Song, Y. Liu, J. Zhao, Experimental study on flow and heat transfer performance of triply periodic minimal surface structures and their hybrid form as disturbance structure, Int. Commun. Heat Mass Tran. 147 (2023) 106942, https://doi.org/10.1016/j.icheatmasstransfer.2023.106942.

[29] M. Modrek, A. Viswanath, K.A. Khan, M.I. Hassan Ali, R.K. Abu Al-Rub, Multi-objective topology optimization of passive heat sinks including self-weight based on triply periodic minimal surface lattices, Case Stud. Therm. Eng. 42 (2023) 102684, https://doi.org/10.1016/j.csite.2022.102684.

[30] E. Gajetti, M. Bonesso, A. Bruschi, F. Fanale, S. Garavaglia, G. Granucci, A. Moro, A. Pepato, A. Romano, L. Savoldi, A new efficient mirror cooling for the transmission line of fusion reactor ECH systems based on triply periodic minimal surfaces, IEEE Trans. Plasma Sci. (2024) 1–7, https://doi.org/10.1109/TPS.2024.3383275.

[31] A. Barakat, B. Sun, Enhanced convective heat transfer in new triply periodic minimal surface structures: numerical and experimental investigation, Int. J. Heat Mass Tran. 227 (2024) 125538, https://doi.org/10.1016/j.ijheatmasstransfer.2024.125538.

[32] C. Piatti, Assessment of Thermal-Hydraulic Performance of Circular Pipes Equipped with Triply Periodic Minimal Surfaces, 2023 Politecnico di Torino.

[33] M.M. Moradmand, A. Sohankar, Numerical and experimental investigations on the thermal-hydraulic performance of heat exchangers with Schwarz-P and gyroid structures, Int. J. Therm. Sci. 197 (2024) 108748, https://doi.org/10.1016/j.ijthermalsci.2023.108748.

[34] J. Iyer, T. Moore, D. Nguyen, P. Roy, J. Stolaroff, Heat transfer and pressure drop characteristics of heat exchangers based on triply periodic minimal and periodic nodal surfaces, Appl. Therm. Eng. 209 (2022) 118192, https://doi.org/10.1016/j.applthermaleng.2022.118192.

[35] J. Li, J. Gonzalez-Aguilar, C. Pérez-Rábago, H. Zeaiter, M. Romero, Optical analysis of a hexagonal 42kWe high-flux solar simulator, Energy Proc. 57 (2014) 590–596, https://doi.org/10.1016/j.egypro.2014.10.213.

[36] J. Li, J. Gonzalez-Aguilar, M. Romero, Line-concentrating flux analysis of 42kWe high-flux solar simulator, Energy Proc. 69 (2015) 132–137, https://doi.org/10.1016/j.egypro.2015.03.016.

[37] S.P.S. Inc., Siemens Digital Industries SoftwareSimcenter STAR-CCM + User Guide V2021, vol. 1, 2021 Siemens, 2021.

[38] D.J. D'Souza, Application of compact flow channel geometries to pressurised solar receivers: a numerical and experimental analysis, PhD Thesis, Universidad Nacional de Educación a Distancia (UNED), 2023.

[39] H. Ebadi, A. Cammi, R. Difonzo, J. Rodríguez, L. Savoldi, Experimental investigation on an air tubular absorber enhanced with Raschig Rings porous medium in a solar furnace, Appl. Energy 342 (2023) 121189.

[40] R. Petela, Exergy of heat radiation, J. Heat Tran. 86 (1964) 187–192, https://doi.org/10.1115/1.3687092.

[41] J.P. Jack, P. Holman, Experimental Methods for Engineers, McGraw-Hill/Connect Learn Succeed, 2012.

[42] B.W. Reynolds, C.J. Fee, K.R. Morison, D.J. Holland, Characterisation of heat transfer within 3D printed TPMS heat exchangers, Int. J. Heat Mass Tran. 212 (2023) 124264, https://doi.org/10.1016/j.ijheatmasstransfer.2023.124264.

[43] S. Catchpole-Smith, R.R.J. Sélo, A.W. Davis, I.A. Ashcroft, C.J. Tuck, A. Clare, Thermal conductivity of TPMS lattice structures manufactured via laser powder bed fusion, Addit. Manuf. 30 (2019) 100846, https://doi.org/10.1016/j.addma.2019.100846.

[44] P.Y. Wang, H.Y. Guan, Z.H. Liu, G.S. Wang, F. Zhao, H.S. Xiao, High temperature collecting performance of a new all-glass evacuated tubular solar air heater with U-shaped tube heat exchanger, Energy Convers. Manag. 77 (2014) 315–323, https://doi.org/10.1016/j.enconman.2013.08.019.

[45] M. Nemś, J. Kasperski, Experimental investigation of concentrated solar air-heater with internal multiple-fin array, Renew. Energy 97 (2016) 722–730, https://doi.org/10.1016/j.renene.2016.06.038.

[46] İ. Türk Toğrul, D. Pehlıvan, The performance of a solar air heater with conical concentrator under forced convection, Int. J. Therm. Sci. 42 (2003) 571–581, https://doi.org/10.1016/S1290-0729(03)00023-1.

[47] R. Tchinda, Thermal behaviour of solar air heater with compound parabolic concentrator, Energy Convers. Manag. 49 (2008) 529–540, https://doi.org/10.1016/j.enconman.2007.08.004.

[48] A. Jasim Mahmood, Thermal evaluation of a double-pass unglazed solar air heater with perforated plate and wire mesh layers, Sustainability 12 (2020), https://doi.org/10.3390/su12093619.

[49] A. Mortazavi, M. Ameri, Conventional and advanced exergy analysis of solar flat plate air collectors, Energy 142 (2018) 277–288, https://doi.org/10.1016/j.energy.2017.10.035.

[50] M.K. Gupta, S.C. Kaushik, Performance evaluation of solar air heater for various artificial roughness geometries based on energy , effective and exergy efficiencies, Renew. Energy 34 (2009) 465–476, https://doi.org/10.1016/j.renene.2008.06.001.

[51] H.H. Öztürk, Y. Demirel, Exergy-based performance analysis of packed-bed solar air heaters, Int. J. Energy Res. 28 (2004) 423–432, https://doi.org/10.1002/er.974.